# A Photometric Study of the Contact Binary GR Piscium

## Edward J. Michaels

*Stephen F. Austin State University, Department of Physics, Engineering, and Astronomy, P. O. Box 13044, Nacogdoches, TX 75962; emichaels@sfasu.edu*

**Abstract**   High-quality CCD photometric light curves of the eclipsing binary GR Psc are presented. The new multicolor light curves display total eclipses which were analyzed using the Wilson-Devinney program. The light curve solution describes the system as a contact configuration with a mass ratio of $M_2/M_1 = 0.431$, a fill-out of f=47%, and a small temperature difference between the component stars of $\Delta T = 51 K$. A period study revealed this A-type contact binary has a decreasing orbital period. A small asymmetry was found in the light curves, indicating an elevated temperature in the contact region of the primary star. This hot region is likely the consequence of mass and energy exchange through the connecting neck of the common envelope.

## 1. Introduction

GR Psc (GSC 01747-00967) was first identified as an eclipsing binary from the All-Sky Automated Survey (ASAS) observations (Pojmański *et al.* 2002). An orbital period of 0.494320 d and a maximum visual magnitude of 11.09 were determined from the ASAS data. The variability of this star was also identified in the Northern Sky Variability Survey (NSVS, Woźniak *et al.* 2004; Nicholson and Varley 2006). Gettel *et al.'s* (2006) catalogue of bright contact binary stars gives an orbital period of 0.494339 d, a visual magnitude of 11.263, and an eclipse amplitude of 0.669 magnitude. Terrell *et al.* (2012) found a color index of (B–V) = 0.404. Gaia DR2 data give a distance of 524 pc and an effective temperature of 6910K (Bailer-Jones *et al.* 2018; Gaia Collaboration 2018).

In this paper, the first photometric study of GR Psc is presented. The photometric observations and data reduction methods are presented in section 2. New times of minima and period analysis are presented in section 3. Analysis of the light curves using the Wilson-Devinney (WD) model is presented in section 4. Discussion of the results and conclusions are presented in section 5.

## 2. Photometric observations

Multi-band photometric observations of GR Psc were acquired in October and November 2019 with the 0.36-m Ritchey-Chrétien robotic telescope located at the Waffelow Creek Observatory (https://obs.ejmj.net). A SBIG-STXL camera equipped with a cooled KAF-6303E CCD (–30°C, 9 μm pixels) was used for imaging. Observations were obtained in four passbands each night, Johnson B and V and Sloan g' and r'. The observation dates and number of images acquired are given in the Table 1 observation log. Nightly bias, dark, and flat frames were acquired for image calibration. MIRA software (Mirametrics 2015) was used for image calibration and the ensemble differential aperture photometry of the light images. The locations of the comparison and check stars are shown in the Figure 1 finder chart. Table 2 lists the comparison and check star coordinates and their standard magnitudes taken from the AAVSO Photometric All-Sky Survey data base (APASS; Henden *et al.* 2015). The GR Psc instrumental magnitudes for each star were converted to standard magnitudes using the APASS comparison star magnitudes. The Heliocentric Julian Date (HJD) of each observation was converted to orbital phase (φ) using the following epoch and orbital period: $T_0 = 2458807.4790$ and P = 0.49431813. The folded light curves for the Johnson B and V passbands are shown in Figure 2 and the Sloan g' and r' in Figure 3. All light curves in this paper were plotted from orbital phase –0.6 to 0.6, with negative phase defined as (φ – 1). Error bars were omitted from the plotted points for clarity. The check star magnitudes were plotted and inspected each night, but no significant variability was found (bottom panels of Figures 2 and 3). The standard deviations for all check star observations are in Table 2.

Table 1. Observation log.

| Filter | Dates | | No. Nights | No. Images |
|--------|-------|---|-----------|-----------|
| B | 2019 Oct 21, 22, 23 | Nov 17, 18, 19 | 6 | 940 |
| V | 2019 Oct 21, 22, 23 | Nov 17, 18, 19 | 6 | 951 |
| Sloan g' | 2019 Oct 21, 22, 23 | Nov 17, 18, 19 | 6 | 962 |
| Sloan r' | 2019 Oct 21, 22, 23 | Nov 17, 18, 19 | 6 | 957 |

Table 2. APASS comparison and check star magnitudes.

| System | R. A. (2000) h | Dec. (2000) ° | B | V | g' | r' |
|--------|---------------|--------------|------|------|------|------|
| GR Psc | 1.158867 | +22.65541 | | | | |
| GSC 01747-00427 (C1) | 1.163354 | +22.69605 | 11.343 | 10.271 | 10.817 | 10.003 |
| GSC 01747-00315 (C2) | 1.154917 | +22.68626 | 11.128 | 10.512 | 10.827 | 10.414 |
| GSC 01747-00927 (C3) | 1.155674 | +22.77302 | 10.823 | 10.212 | 10.579 | 10.081 |
| GSC 01747-00409 (K) | 1.166047 | +22.73883 | 11.948 | 10.948 | 11.428 | 10.725 |
| Standard deviation of observed K-star magnitudes | | | ± 0.011 | ± 0.007 | ± 0.008 | ± 0.006 |

Table 3. Average light curve properties.

|   | Min I Mag. | Min II Mag. | Δ Mag. Min II – Min I | Max I Mag. | Max II Mag. | Δ Mag. Max II – Max I | Mag. Range Max II – Min I |
|---|---|---|---|---|---|---|---|
| B | 12.244 ±0.003 | 12.155 ±0.002 | -0.089 ±0.003 | 11.514 ±0.002 | 11.500 ±0.002 | -0.015 ±0.003 | 0.744 ±0.003 |
| V | 11.786 ±0.002 | 11.708 ±0.002 | -0.077 ±0.003 | 11.089 ±0.002 | 11.078 ±0.002 | -0.012 ±0.002 | 0.708 ±0.002 |
| g' | 12.046 ±0.004 | 11.970 ±0.004 | -0.076 ±0.006 | 11.342 ±0.004 | 11.326 ±0.004 | -0.016 ±0.006 | 0.720 ±0.006 |
| r' | 11.736 ±0.004 | 11.672 ±0.004 | -0.064 ±0.005 | 11.057 ±0.004 | 11.050 ±0.004 | -0.007 ±0.005 | 0.686 ±0.005 |

*Secondary Total Eclipse Duration: 21.3 ± 0.2 minutes.*

The standard error of a single observation ranged from 5 to 10 mmag. Each light curve shows a flat secondary minimum, indicating a total eclipse. The light curve properties for each passband are given in Table 3 (Min I, Min II, Max I, Max II, Δm, and total eclipse duration). The observations can be accessed from the AAVSO International Database (Kafka 2017).

## 3. Period study and ephemerides

From the observations, seven new minima timings were determined using the Kwee and van Woerden (1956) method. Four minima timings were available for each eclipse, one from each of the four passbands observed (B, V, g', r'). No significant offsets were found between the timings in each set. The minimum for each eclipse was computed by averaging the four timings. The new times of minima are collected in Table 4, along with additional eclipse timings found in the literature.

The initial ephemeris used to calculate the O–C residuals in Table 4 was taken from the International Variable Star Index (VSX; Watson *et al.* 2006):

$$\text{HJD Min I} = 2452856.8533 + 0.494320\ E. \qquad (1)$$

The O–C residuals of Equation 1 are shown in the top panel of Figure 4. The general trend of the residuals indicates the orbital period of GR Psc is continuously decreasing. A least-squares solution to the residuals of Equation 1 gives the following quadratic ephemeris:

$$\text{HJD Min I} = 2458807.4790(4) + 0.4943181(2)\ E$$
$$- 1.67(8) \times 10^{-10}\ E^2. \quad (2)$$

The rate of period change for this solution is $dP/dt = -2.5(1) \times 10^{-7}\ d\ yr^{-1}$, about 2.1 seconds per century. The best-fit quadratic line from Equation 2 is the solid line in the middle panel of Figure 4, with the residuals shown in the bottom panel.

An updated linear ephemeris was computed by least-squares using the residuals of Equation 1 is given by:

$$\text{HJD Min I} = 2458807.479(2) + 0.4943188(1)\ E. \qquad (3)$$

Due to the changing period of this star, only the most recent

Table 4. Times of minima and O–C residuals.

| Epoch HJD 2400000+ | Error | Cycle | O–C | References |
|---|---|---|---|---|
| 51467.80630 | — | –2810.0 | 0.00780 | Nicholson and Varley (2006) |
| 52856.85330 | — | 0.0 | 0.00000 | GCVS (Samus *et al.* 2017), VSX (Watson *et al.* 2014) |
| 55528.66030 | 0.00010 | 5405.0 | 0.00740 | Diethelm (2011) |
| 55577.35080 | — | 5503.5 | 0.00738 | Nagai (2012) |
| 55585.25800 | — | 5519.5 | 0.00546 | Nagai (2012) |
| 55805.48000 | 0.00030 | 5965.0 | 0.00790 | Hübscher and Lehman (2013) |
| 55818.57890 | 0.00100 | 5991.5 | 0.00732 | Banfi *et al.* (2012) |
| 55859.36060 | 0.00010 | 6074.0 | 0.00762 | Hübscher and Lehman (2013) |
| 55894.70210 | 0.00040 | 6145.5 | 0.00524 | Diethelm (2012) |
| 56558.82180 | 0.00020 | 7489.0 | 0.00602 | Samolyk (2015) |
| 56578.10010 | — | 7528.0 | 0.00584 | Nagai (2014) |
| 56952.79470 | 0.00020 | 8286.0 | 0.00588 | Samolyk (2015) |
| 57703.66490 | 0.00010 | 9805.0 | 0.00400 | Samolyk (2017) |
| 58050.67770 | 0.00010 | 10507.0 | 0.00416 | Samolyk (2018) |
| 58369.51249 | 0.00005 | 11152.0 | 0.00255 | Ozavci *et al.* (2019) |
| 58778.80858 | 0.00019 | 11980.0 | 0.00168 | present paper |
| 58779.79751 | 0.00019 | 11982.0 | 0.00197 | present paper |
| 58780.78610 | 0.00020 | 11984.0 | 0.00192 | present paper |
| 58803.77171 | 0.00008 | 12030.5 | 0.00165 | present paper |
| 58805.74886 | 0.00024 | 12034.5 | 0.00152 | present paper |
| 58806.73795 | 0.00023 | 12036.5 | 0.00197 | present paper |
| 58807.72602 | 0.00018 | 12038.5 | 0.00140 | present paper |

minima times (2016–2019) were used in this solution. The best-fit linear line from Equation 3 is the solid line segment shown in the top panel of Figure 4. This new linear ephemeris should be useful for predicting future primary eclipse times but will need to be updated frequently.

## 4. Analysis

### 4.1. Color, temperature, spectral type, absolute magnitude, luminosity

To determine the observed color of this system, the large number of observations (over 900 in each passband) were binned in both phase and magnitude with a phase width of 0.01. The phases and magnitudes in each bin were averaged. Figure 5 shows the resulting binned V light curve and the (B–V) color curve (bottom panel). The average observed color over the entire phase range is (B–V) = 0.438 ± 0.009. The color excess for this system, E(B–V) = 0.035 ± 0.018, was determined from

dust maps based on Pan-STARRS 1 and 2MASS photometry and Gaia parallaxes (Green *et al.* 2018). A small color excess for this system is not unexpected, given its low galactic latitude (b = –41°) and proximity to Earth. The distance, d = $524^{25}_{23}$ pc, was determined from the Gaia DR2 parallax (Bailer-Jones *et al.* 2018; Gaia 2016, 2018). Subtracting the color excess from the average observed color gives an intrinsic color of $(B–V)_o$ = 0.40 ± 0.02.

A spectroscopically determined temperature is not available for this star. A machine-learning regression analysis using Gaia DR2 data, combined with data from four spectroscopic surveys, gives a temperature of $T_{eff}$ = 6811 ± 145 K, and a spectral type of F2 (Bay *et al.* 2019; Pecaut and Mamajek 2013). This temperature will be assigned to the primary star for light curve modeling in section 4.2.

### 4.2. Light curve modeling

Light curve solutions were obtained using the 2015 version of the Wilson-Devinney (WD) program where computations were done simultaneously in all four passbands (Wilson and Devinney 1971; Van Hamme and Wilson 1998). For input data, the observed standard magnitudes were binned in both phase and magnitude (see section 4.1). For each color, 100 normal points were formed from the observations. For WD modeling, these magnitude normal points were converted to normalized flux, with each point assigned a weight equal to the number of observations forming that point.

The light curves are smoothly varying and have similar minima depths, which suggests the stars are in a contact configuration with a common convective envelope. The WD program was therefore configured for overcontact binaries (Mode 3). The Kurucz stellar atmosphere model was applied (Kurucz 2002). The primary star's effective temperature was fixed at $T_1$ = 6811 K (see section 4.1). The subscripts 1 and 2 refer to the hotter and cooler components, respectively. With the effective temperature below 7200 K, standard convective parameters were used: gravity brightening, $g_1 = g_2 = 0.32$ (Lucy 1968) and bolometric albedo value $A_1 = A_2 = 0.5$ (Ruciński 1969). Logarithmic limb darkening coefficients were calculated by the program from tabulated values using the method of Van Hamme (1993). The adjustable parameters include the inclination (i), mass ratio ($q = M_2 / M_1$), potential ($\Omega_1 = \Omega_2$), temperature of the secondary star ($T_2$), the band-specific luminosity for each wavelength (L), third light (l), and phase shift. Since no spectroscopic mass ratio is currently available for the system, a search for the solution was made using several fixed values of mass ratio. The results of this q-search gave a clear residual minimum at about q = 0.430 (see Figure 6). This value was used as the starting mass ratio for the final solution iterations where the mass ratio was an adjustable parameter. The final best-fit solution parameters are shown in column 2 of Table 5. The filling-factor was computed using the method of Lucy and Wilson (1979) given by:

$$f = \frac{\Omega_{inner} - \Omega}{\Omega_{inner} - \Omega_{outer}}, \qquad (4)$$

where $\Omega_{inner}$ and $\Omega_{outer}$ are the inner and outer critical equipotential

Table 5. Results derived from light curve modeling.

| Parameter | No Spot | Spot |
|---|---|---|
| *f* (filling factor) | 48% | 47% |
| i (°) | 83.8 ± 0.4 | 83.9 ± 0.3 |
| $T_1$ (K) | [1]6811 | [1]6811 |
| $T_2$ (K) | 6762 ± 5 | 6760 ± 4 |
| $\Omega_1 = \Omega_2$ | 2.619 ± 0.010 | 2.619 ± 0.009 |
| q (M2/M1) | 0.433 ± 0.008 | 0.431 ± 0.006 |
| $L_1/(L_1+L_2)$ (B) | 0.680 ± 0.012 | 0.682 ± 0.010 |
| $L_1/(L_1+L_2)$ (V) | 0.678 ± 0.012 | 0.680 ± 0.010 |
| $L_1/(L_1+L_2)$ (g') | 0.679 ± 0.012 | 0.681 ± 0.010 |
| $L_1/(L_1+L_2)$ (r') | 0.677 ± 0.011 | 0.679 ± 0.010 |
| $r_1$ side | 0.4832 ± 0.0008 | 0.4814 ± 0.0008 |
| $r_2$ side | 0.3409 ± 0.0074 | 0.3452 ± 0.0061 |

| Spot | Star[1] |
|---|---|
| colatitude (°) | 98 ± 5 |
| longitude (°) | 4 ± 2 |
| spot radius (°) | 19 ± 2 |
| temp. factor | 1.06 ± 0.02 |

*[1] Assumed.*

*The subscripts 1 and 2 refer to the star being eclipsed at primary and secondary minimum, respectively.*

*Note: The errors in the stellar parameters result from the least-squares fit to the model. The actual uncertainties are considerably larger.*

surfaces and $\Omega$ is the equipotential that describes the stellar surface. When third light was included in the adjustable parameters, only negligibly small or negative values resulted. This indicates there is no detectable third light contribution to the system light. The solution also did not find a phase-shift necessary to fit the observations; they had been accurately phased by the ephemeris. Figure 7 shows the normalized light curves for each passband overlaid by the synthetic solution curves (solid lines), and with the residuals shown in the bottom panel.

### 4.3. Spot model

The light curves of GR Psc are not perfectly symmetric, as evidenced by the small O'Connell effect. In each light curve, the peak magnitude following secondary minimum (Max II, φ = 0.75) is slightly brighter than the maximum following the primary eclipse (Max I, φ = 0.25). The small differences in the peak magnitudes for each color (Δm) are given in Table 3. The O'Connell effect is generally attributed to hot or cool spots on one or both stars. Light curve asymmetries are often difficult to detect by visual inspection. To better characterize the asymmetries in the GR Psc light curves, an analysis was performed on the normalized flux points using a truncated twelve-term Fourier fit given by:

$$I(\varphi) = a_0 + \sum_{(n=1)}^{12} (a_n \cos(2\pi n\varphi) + b_n \sin(2\pi n\varphi)), \qquad (5)$$

where I(φ) is the flux at phase φ and $a_0$, $a_n$, and $b_n$ are the Fourier coefficients (Wilsey and Beaky 2009; Akiba *et al.* 2019). Figure 8 shows the Fourier fits to the normalized flux points for each color. In Figure 9 the two halves of the B light curve are superimposed to reveal the asymmetries. The bottom panel shows the difference in normalized flux, ΔI(φ), for each color.

The asymmetry is color dependent, with the B and g′ light curves showing the most deviation and the r′ curve the least. Assuming the asymmetries are caused by star spots, these flux differences indicate a possible hot spot on the primary star, near to but not centered at the contact region of the two stars. The excess light seen in the light curve solution near orbital phase $\varphi = 0.80$ also supports a hot spot near this location (see Figure 7).

The program BINARY MAKER 3.0 (BM3) was used to model a hot spot near the neck region of the primary star (Bradstreet and Steelman 2002). The initial orbital and stellar parameters were taken from the WD spotless model with the addition of the spot parameters: colatitude, longitude, spot radius, and temperature factor ($T_s /T_{eff}$). The spot values were adjusted until a good fit resulted between the synthetic and observed light curves. A new WD solution was then obtained using the spot parameters from the BM3 fit. The best-fit WD spotted solution parameters are shown in column 3 of Table 5. Figure 10 shows the final spotted model fits (solid lines) to the observed light curves with the residuals shown in the bottom panel. The fit improved considerably for this solution with the residuals 28% lower than the spotless model. BM3 generated a graphical representation of the spot model shown in Figure 11.

## 5. Discussion and conclusions

The secondary total eclipse of GR Psc provided the necessary constraints for a well determined mass ratio (Wilson 1978; Terrell and Wilson 2005). The WD solution mass ratio, combined with an estimate for the primary star's mass, were used to calculate provisional absolute stellar parameters for this system. The primary mass was calculated using the Gazeas and Stępień (2008) period-mass relation for contact binaries,

$$\log M_1 = (0.755 \pm 0.059) \log P + (0.416 \pm 0.024), \quad (6)$$

where P is the orbital period. Equation 8 gives a primary star mass of $M_1 = 1.5 \pm 0.1 \, M_\odot$. The secondary star's mass, $M_2 = 0.66 \pm 0.05 \, M_\odot$, was determined using the mass ratio. The primary star of a contact binary is typically on the main sequence, providing a second method for estimating its mass. Using the primary's effective temperature, the mass was interpolated from the tables of Pecaut and Mamajek (2013), giving a value of $1.44 \, M_\odot$. The two values are in good agreement, differing by only 4%. The separation between the mass centers of the stars was calculated using Kepler's Third Law. Using the spotted solution parameters, the WD light curve program (LC) computed the mean radius and bolometric magnitude ($M_{bol}$) of each star. The stellar luminosities were calculated using the following equation:

$$M_{bol} = 4.74 - 2.5 \log (L/L_\odot) . \quad (7)$$

The calculated stellar masses, radii, luminosities, and the semi-major axis are collected in Table 6.

The nonlinear O–C variations in the orbital periods of eclipsing binaries are caused by mass loss from the system, third bodies, or mass transfer between the component stars.

Table 6. Provisional absolute parameters.

| Parameter | Symbol | Value |
|---|---|---|
| Stellar masses | $M_1 \, (M_\odot)$ | $1.5 \pm 0.1$ |
| | $M_2 \, (M_\odot)$ | $0.66 \pm 0.05$ |
| Semi-major axis | $a \, (R_\odot)$ | $3.42 \pm 0.08$ |
| Mean stellar radii | $R_1 \, (R_\odot)$ | $1.66 \pm 0.03$ |
| | $R_2 \, (R_\odot)$ | $1.17 \pm 0.03$ |
| Bolometric magnitude | $M_{bol,1}$ | $2.93 \pm 0.09$ |
| | $M_{bol,2}$ | $3.72 \pm 0.12$ |
| Stellar luminosity | $L_1 \, (L_\odot)$ | $5.4 \pm 0.4$ |
| | $L_2 \, (L_\odot)$ | $2.6 \pm 0.3$ |

*The calculated values in this table are provisional. Radial velocity observations are necessary for direct determination of M1, M2, and a.*

The decreasing orbital period of GR Psc may be the result of magnetic braking, but the apparent lack of dark spots on the stars indicates little magnetic activity at the current time. Light-time effects could also cause apparent orbital period change due to the binary pair orbiting a third body. In this case the observed period change may be a small part of a sinusoidally varying ephemeris. No appreciable third light was found in the WD light curve solutions, but this does not preclude a third, very low luminosity star in the system. Additional minima timings over many years will be necessary to determine if GR Psc is a trinary system. Given this system's contact configuration, the decreasing orbital period could also be caused by conservative mass exchange from the primary star to the less massive secondary. Using the rate of period change computed in section 2 and the estimated stellar masses gives a mass transfer rate of $-5.3(2) \times 10^{-10} \, M_\odot / day$. The matter and energy exchange through the neck of the common envelope would explain the higher local temperature found in this region (Van Hamme and Wilson 1985). Additional supporting evidence for the location of this hot region can be seen in the Figure 5 color plot. The system light is slightly bluer at the orbital phases that provide the best direct line-of-sight to the hot spot, at approximately $\varphi = 0.2$ and $\varphi = 0.8$ (see Figure 11). The light is reddened a small amount at primary eclipse as the secondary star transits the slightly hotter primary star and blocks from view the hot spot in the neck region.

GR Psc is an A-type W UMa contact binary where the primary eclipse is a transit of the larger star by the smaller and slightly cooler secondary component (Binnendijk 1970). The best-fit WD spotted solution gives a temperature difference between the component stars of only 51 K, a mass ratio of $M_2 / M_1 = 0.431$, and a moderate degree of contact with a filling factor of 47%. A period analysis indicates a decreasing orbital period likely caused by mass exchange. The hot spot modeled in the neck region of the primary star is not unexpected, given the energy exchange that must occur between the stars. To confirm the provisional absolute stellar parameters presented here, a future spectroscopic study of this system would be invaluable.

## 6. Acknowledgements

# References

Akiba, T., Neugarten, A., Ortmann, C., and Gokhale, V. 2019, *J. Amer. Assoc. Var. Star Obs.*, **47**, 186.

Bailer-Jones, C., Rybizki, J., Fouesneau, M., Mantelet, G., and Andrae, R. 2018, *Astron. J.*, **156**, 58.

Banfi, M., *et al.* 2012, *Inf. Bull. Var. Stars*, No. 6033, 1.

Bay, Y., Liu, J.-F.g, Bai, Z.-R., Wang, S., and Fan, D.-W. 2019, *Astron. J.*, **158**, 93.

Binnendijk, L. 1970, *Vistas Astron.*, **12**, 217.

Bradstreet, D. H., and Steelman, D. P. 2002, *Bull. Amer. Astron. Soc.*, **34**, 1224.

Diethelm, R. 2011, *Inf. Bull. Var. Stars*, No. 5960, 1.

Diethelm, R. 2012, *Inf. Bull. Var. Stars*, No. 6011, 1.

Gaia Collaboration, *et al.* 2016, *Astron. Astrophys.*, **595A**, 1.

Gaia Collaboration, *et al.* 2018, *Astron. Astrophys.*, **616A**, 1.

Gazeas, K., and Stępień, K., 2008, *Mon. Not. Roy. Astron. Soc.*, **390**, 1577.

Gettel, S. J., Geske, M. T., and McKay, T. A. 2006, *Astron. J.*, **131**, 621.

Green, G. M., *et al.* 2018, *Mon. Not. Roy. Astron. Soc.*, **478**, 651.

Henden, A. A., *et al.* 2015, AAVSO Photometric All-Sky Survey, data release 9, (https://www.aavso.org/apass).

Hübscher, J., and Lehmann, P. B. 2013, *Inf. Bull. Var. Stars*, No. 6070, 1.

Kafka, S. 2017, variable star observations from the AAVSO International Database (https://www.aavso.org/aavso-international-database).

Kurucz, R. L. 2002, *Baltic Astron.*, **11**, 101.

Kwee, K. K., and van Woerden, H. 1956, *Bull. Astron. Inst. Netherlands*, **12**, 327.

Lucy, L. B., 1968, *Astrophys. J.*, **151**, 1123.

Lucy, L. B., and Wilson, R. E. 1979, *Astrophys. J.*, **231**, 502.

Mirametrics. 2015, Image Processing, Visualization, Data Analysis, (https://www.mirametrics.com).

Nagai, K. 2012, *Bull. Var. Star Obs. League Japan*, No. 53, 1.

Nagai, K. 2014, *Bull. Var. Star Obs. League Japan*, No. 56, 1.

Nicholson, M. and Varley, H. 2006, *Inf. Bull. Var. Stars*, No. 5700, 16.

Ozavci, I., *et al.* 2019, *Open Eur. J. Var. Stars*, **203**, 1.

Pecaut, M. J., and Mamajek, E. E. 2013, *Astrophys. J., Suppl. Ser.*, **208**, 9 (http://www.pas.rochester.edu/~emamajek/EEM_dwarf_UBVIJHK_colors_Teff.txt).

Pojmański, G. *et al.* 2002, *Acta Astron.*, **52**, 397.

Ruciński, S. M. 1969, *Acta Astron.*, **19**, 245.

Samolyk, G. 2015, *J. Amer. Assoc. Var. Star Obs.*, **43**, 77.

Samolyk, G. 2017, *J. Amer. Assoc. Var. Star Obs.*, **45**, 121.

Samolyk, G. 2018, *J. Amer. Assoc. Var. Star Obs.*, **46**, 184.

Samus N. N., Kazarovets E. V., Durlevich O. V., Kireeva N. N., and Pastukhova E. N. 2017, *Astron. Rep.*, **61**, 80 (*General Catalogue of Variable Stars: Version GCVS 5.1*, http://www.sai.msu.su/groups/cluster/gcvs/gcvs).

Terrell, D., Gross, J., and Cooney, W. R. 2012, *Astron. J.*, **143**, 99.

Terrell, D., and Wilson, R. E. 2005, *Astrophys. Space Sci.*, **296**, 221.

van Hamme, W. 1993, *Astron. J.*, **106**, 2096.

van Hamme, W., and Wilson, R. E. 1985, *Astron. Astrophys.*, **152**, 25.

van Hamme, W., and Wilson, R. E. 1998, *Bull. Amer. Astron. Soc.*, **30**, 1402.

Watson, C., Henden, A. A., and Price, C. A. 2014, AAVSO International Variable Star Index VSX (Watson+, 2006–2014; http://www.aavso.org/vsx).

Wilsey N. J., and Beaky M. M. 2009, in *The Society for Astronomical Sciences 28th Annual Symposium on Telescope Science*, The Society for Astronomical Sciences, Rancho Cucamonga, Calif, 107.

Wilson, R. E. 1978, *Astrophys. J.*, **224**, 885.

Wilson, R. E., and Devinney, E. J., 1971, *Astrophys. J.*, **166**, 605.

Woźniak, P. R., *et al.* 2004, *Astron. J.*, **127**, 2436.
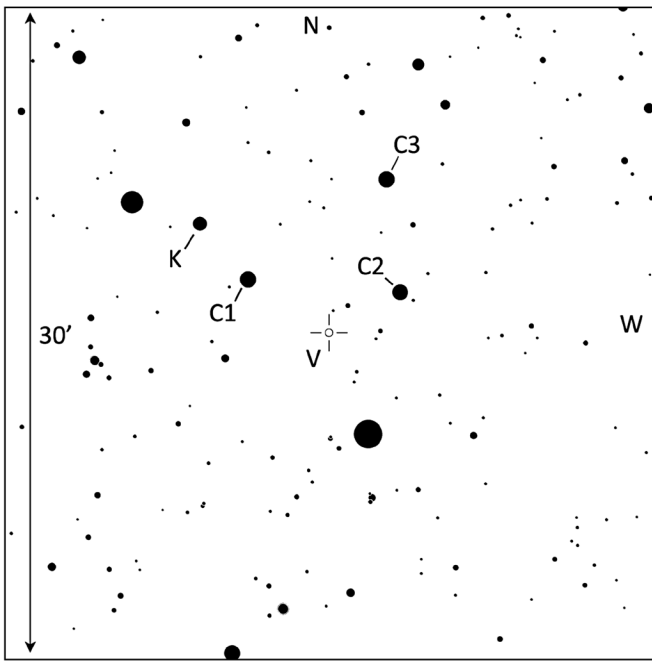
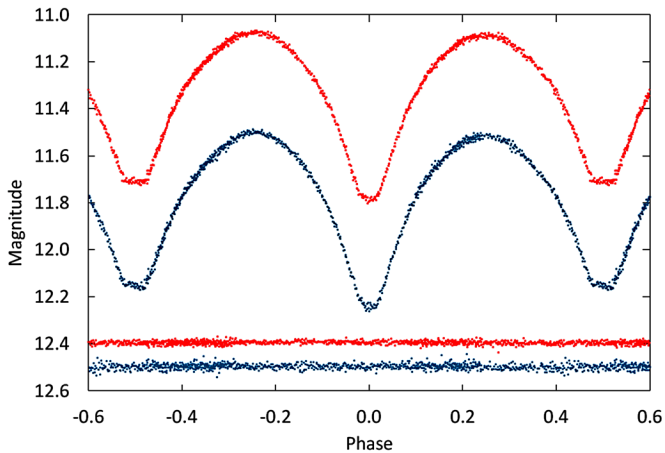Figure 1. Finder chart for GR Psc (V), comparison (C1–C3), and check (K) stars.



Figure 2. The observed Johnson B and V light curves in standard magnitudes. The bottom curves are the Johnson B and V check star magnitudes offset +0.52 and +1.42 magnitudes, respectively. For both sets of curves, the top curve is Johnson V and the bottom curve is Johnson B.
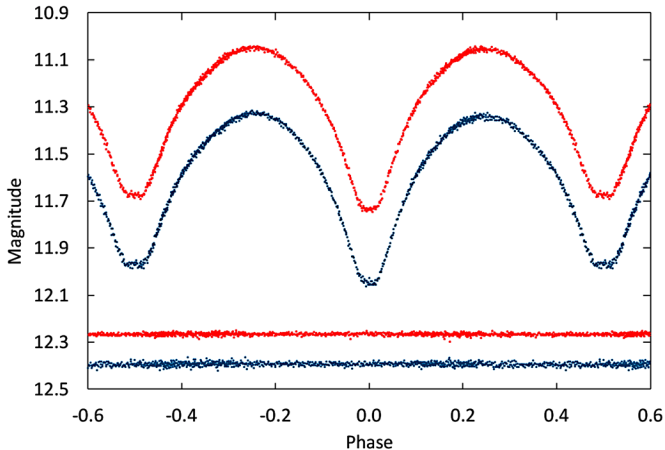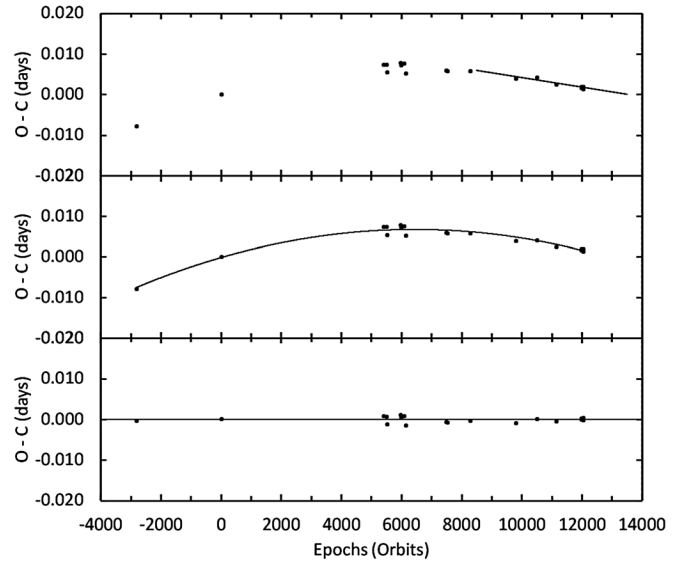


Figure 3. The observed Sloan g' and r' light curves in standard magnitudes. The bottom set of curves are the Sloan g' and r' check star magnitudes offset by +0.90 and 1.60, respectively. For both sets of curves, the top curve is Sloan r' and the bottom curve is Sloan g'.



Figure 4. The top panel shows the residuals (dots) calculated from the linear ephemeris of Equation 1. The solid line segment is the best-fit linear line from Equation 3 using minima times from 2016 to 2019. The middle panel shows the O–C residuals from Equation 1 with the solid line the quadratic ephemeris fit from Equation 2. The bottom panel shows the residuals after removing the downward parabolic change.
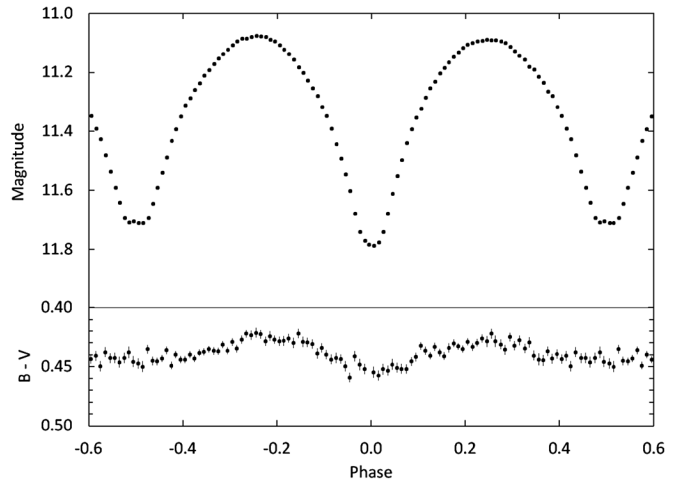


Figure 5. Light curve of all V band observations in standard magnitudes (top panel). The observations were binned with a phase width of 0.01. The errors for each binned point are about the size of the plotted points. The B–V colors were calculated by subtracting the linearly interpolated binned B and V magnitudes.
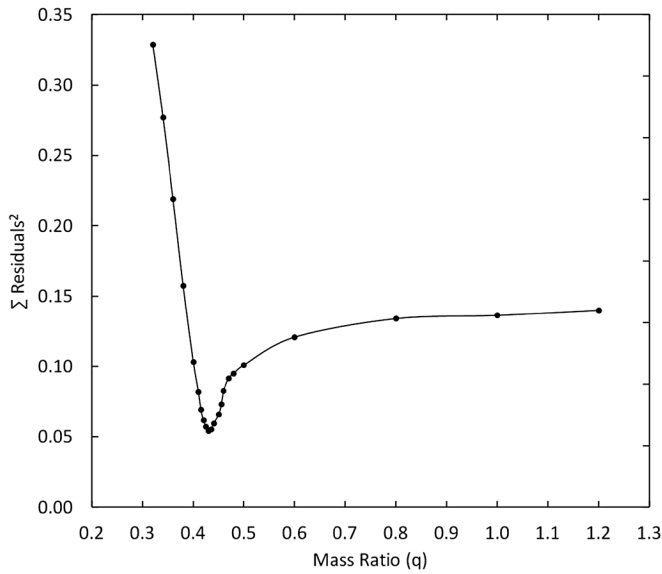
Figure 6. Results of the q-search showing the relation between the sum of the residuals squared and the mass ratio (q).
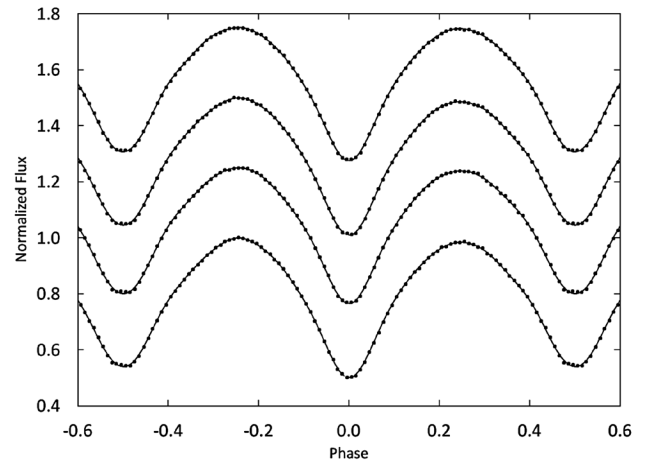


Figure 8. The normalized flux for GR Psc. From top to bottom the plotted points correspond to the r' g' V B filters. The Fourier fits are the solid lines. Each curve is offset by 0.25 for this combined plot. Error bars are omitted from the points for clarity.
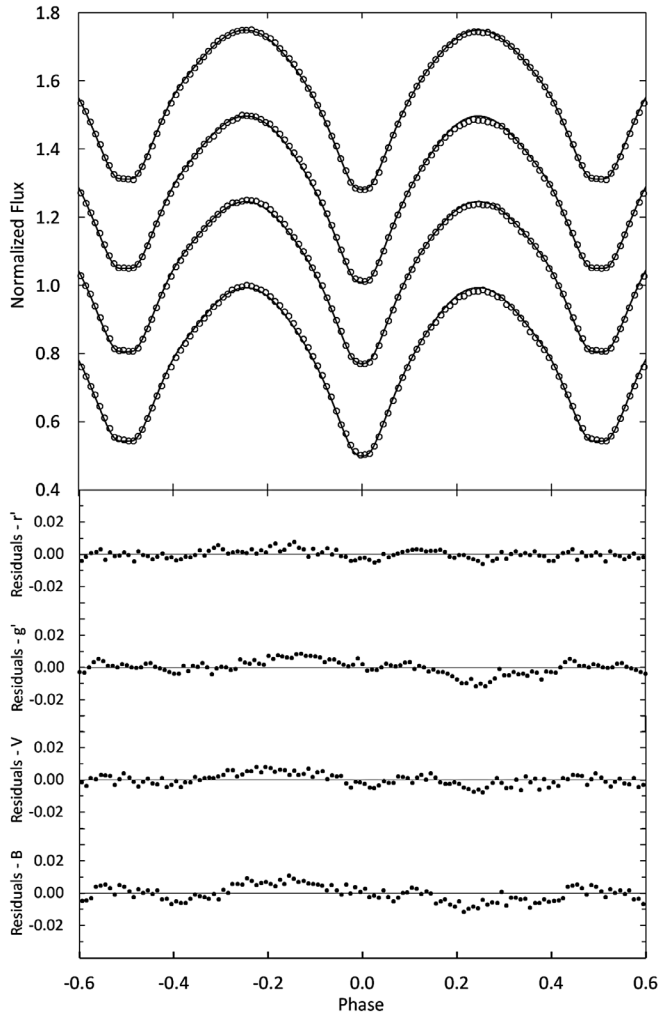


Figure 7. Comparison between the WD spotless best-fit model (solid curve) and the observed normalized flux curve. From top to bottom the filters are r' g' V B. Each light curve is offset by 0.25 for this combined plot. The residuals are shown in the bottom panel. Error bars are omitted from the points for clarity.
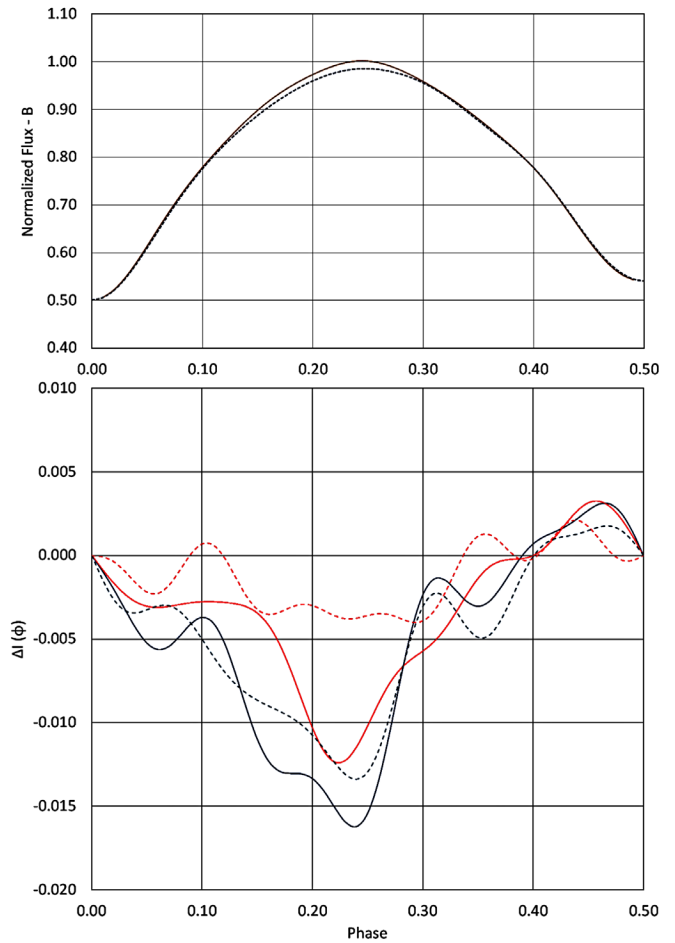


Figure 9. The top panel superimposes the two halves of the B light curve to reveal the light curve asymmetries. The dashed line is orbital phase (φ) 0.0 to 0.5, and the solid line 0.5–1.0. The bottom panel shows the differences between the two halves of the light curve for each color. The solid blue line is the B filter, the solid red line the V, the dashed blue line the g', and the dashed red line the r'.
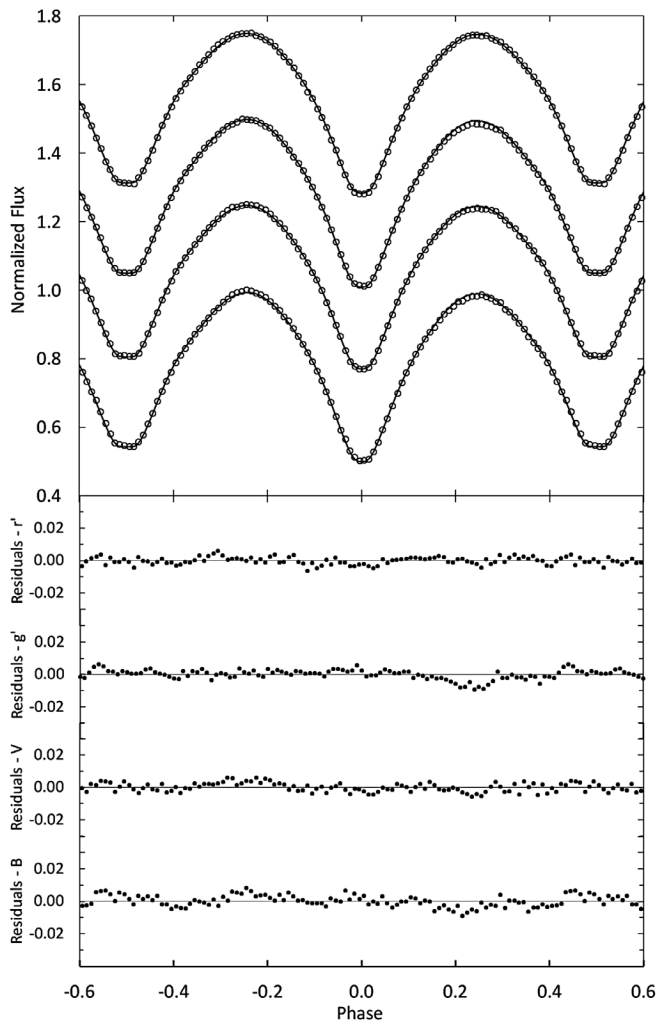
Figure 10. Comparison between the WD spotted best-fit model (solid curve) and the observed normalized flux curve. From top to bottom the filters are r' g' V B. Each light curve is offset by 0.25 for this combined plot. The residuals are shown in the bottom panel. Error bars are omitted from the points for clarity.
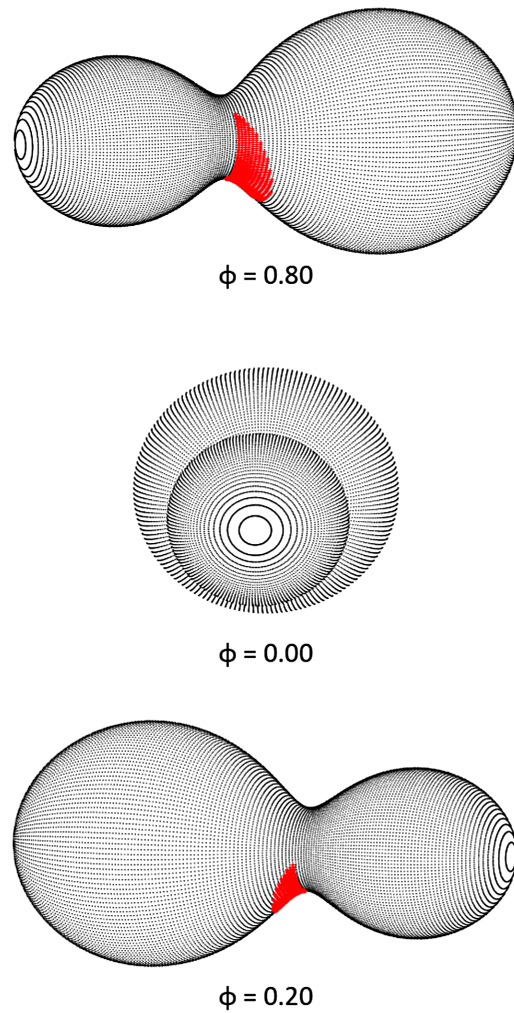


Figure 11. Roche Lobe surfaces of the best-fit WD spot model showing spot locations. The orbital phase is shown below each diagram.